



Phase transformation and incompatibility at grain boundaries in zirconia-based shape memory ceramics: a micromechanics-based simulation study

Zhiyi Wang^{1,3}, Alan Lai², Christopher A. Schuh², and Raúl Radovitzky^{1,3,*} 

¹Department of Aeronautics and Astronautics, Massachusetts Institute of Technology, 77 Mass. Ave, Cambridge, MA 02139, USA

²Department of Materials Science and Engineering, Massachusetts Institute of Technology, 77 Mass. Ave, Cambridge, MA 02139, USA

³Institute for Soldier Nanotechnologies, Massachusetts Institute of Technology, 77 Mass. Ave, Cambridge, MA 02139, USA

Received: 4 March 2022

Accepted: 5 May 2022

Published online:

16 June 2022

© The Author(s) 2022

ABSTRACT

Zirconia-based shape memory ceramics (SMCs) exhibit anisotropic mechanical response when undergoing elastic deformations as well as during austenite–martensite phase transformation. This behavior results in different types of strain incompatibility at grain boundaries, which we study here using a micromechanical model. A single-crystal model is implemented to provide a full mechanistic three-dimensional description of the anisotropic elastic as well as martensitic transformation stress–strain response, including non-Schmid behavior caused by the significant volume change during martensitic transformation. This model was calibrated to and validated against compression tests of single-crystal zirconia micro-pillars conducted previously, and then used to model bi-crystals. Upon the introduction of a grain boundary, the simulation provides detailed information on the nucleation and evolution of martensite variants and stress distribution at grain boundaries. We identify bi-crystal configurations which result in very large stress concentrations at very low deformations due to elastic incompatibility, as well as others where the elastic incompatibility is relatively low and stress concentrations only occur at large transformation strains. We also show how this approach can be used to explore the misorientation space for quantifying the level of elastic and transformation incompatibility at SMCs grain boundaries.

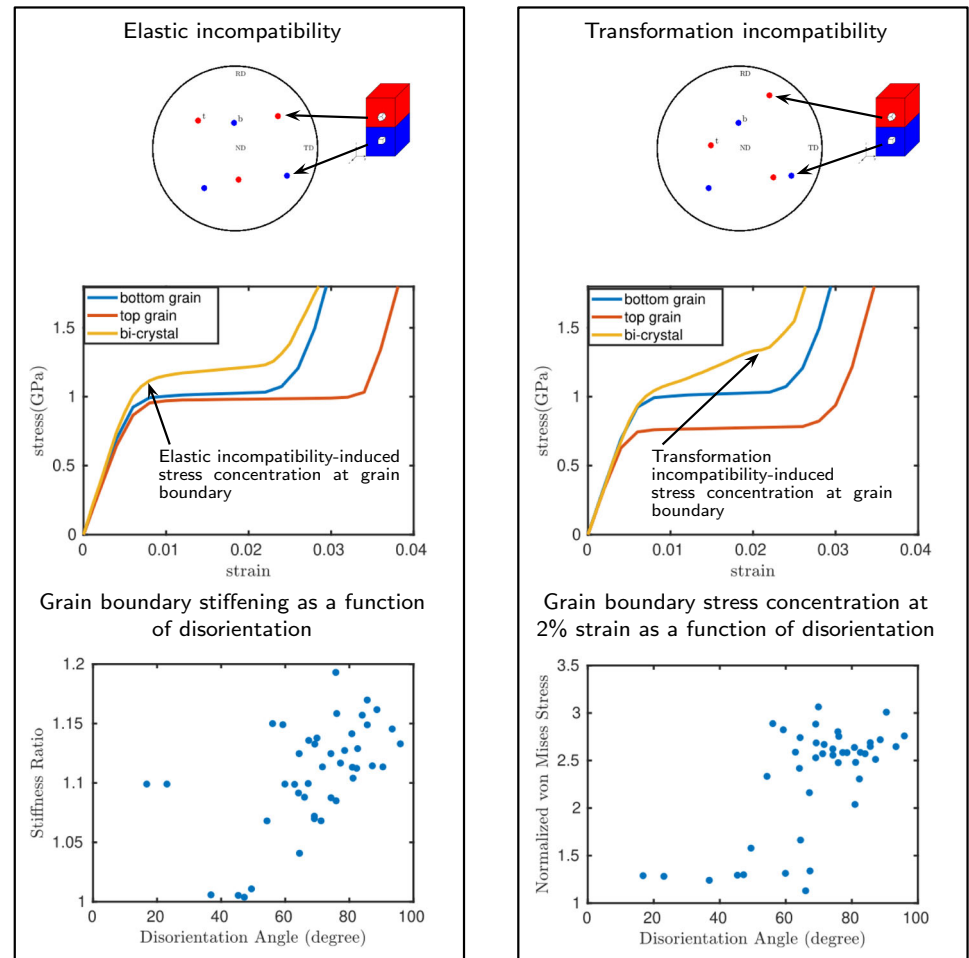
Handling Editor: Catalin Croitoru.

Address correspondence to E-mail: rapa@mit.edu

E-mail Addresses: kellywzy@mit.edu; alanlai@mit.edu; schuh@mit.edu

GRAPHICAL ABSTRACT

Micromechanics models provide insights on grain boundary elastic and phase transformation strain incompatibility in shape memory zirconia



Introduction

By virtue of a reversible martensitic transformation, shape memory materials are able to recover their original shape upon heating, and can exhibit superelasticity—reversible large strains accommodated by the transformation. Recent work [1–6] has expanded the study of shape memory from metals to martensitic ceramics, with significant attention on zirconia-based shape memory ceramics (SMCs). At the crystal level, SMCs can undergo reversible diffusionless solid-to-solid phase transformations from

austenite to martensite similar to those observed in metallic shape memory materials, while also having much higher hardness, transformation stress, transformation temperature, and transformation hysteresis. These unique properties are promising for various applications. Large transformation stresses on the order of GPa are expected to translate into large output stresses when used for actuator applications [7]. High melting and transformation temperatures make SMCs viable for high-temperature applications. The ability to dissipate significant amounts of energy makes them desirable materials for force protection and shielding purposes.

However, polycrystalline zirconia-based ceramics are known to suffer from premature fracture at very small strain levels resulting in very limited superelastic cycling [8]. This embrittlement problem has severely limited the application of these materials in practical situations. It has been recently demonstrated that when made into small volumes or single-crystal forms, zirconia-based SMCs can avoid such catastrophic cracking [1, 6]. For example, Lai et al. manufactured zirconia micro-pillars that are able to withstand dozens of transformation cycles at significant strain levels of several percent, indicating great improvement over polycrystalline superelastic zirconia [1]. Large (cm-scale) single crystals of SMC also exhibit highly reversible transformation behavior over many cycles [9].

The issue of stress concentration and potential intergranular fracture due to grain boundary constraints is well studied in polycrystalline metals including shape memory alloy (SMAs). Extensive studies have been conducted using models of crystal plasticity to understand the role of microstructure attributes such as grain orientation, grain boundary characteristics, and specimen texture on deformation and failure mechanism at polycrystalline grain boundaries [10–15]. In the case of SMAs, previous work has investigated the tendency of Cu-based SMAs to fracture along grain boundaries due to strain incompatibilities there [16–18]. In SMCs, grain boundary strain incompatibility is less studied, although recent work has provided significant insights [9, 19–21]. Pang et al. [19] investigated the two-dimensional compatibility of the martensite-austenite interface via the application of the cofactor conditions as a possible factor controlling the cracking of bulk polycrystalline zirconia-based SMCs. Their results suggested that samples with excellent interface compatibility could avoid cracking during thermal cycles and bulk compatibility is not necessarily the dominant cause of transformation-induced fracture. The same authors [20] analyzed the differences in thermally-induced transformation behaviors between $\text{ZrO}_2\text{-CeO}_2$ oligocrystalline powders and sintered pellets. The role of grain boundaries in the damage evolution of yttria-doped zirconia subject to thermal cyclic loading was also discussed in [9, 21]. However, these works focused on the thermally triggered transformation, which involves more degrees of freedom in the selection of transformation variants as compared with a stress-triggered

transformation such as is relevant for superelasticity. The main goal of this paper is to improve our understanding of the sources of grain boundary incompatibility in zirconia-based SMCs. This can help identify grain boundary configurations that increase the superelastic range of SMCs in polycrystalline form.

The martensitic phase transformation in zirconia comprises a shear distortion as well as a significant volume change, which is far larger than typical in SMAs [9, 19, 22, 23]. Similar to shape memory alloys, micromechanical features of martensite, including the transformation systems (habit plane normal and transformation direction), can be identified by the geometrically nonlinear theory of martensite [24–27]. In the case of SMAs, there have been significant efforts in developing continuum models of martensitic transformation with micromechanical descriptions of deformation at the crystal level [28–32]. In order to incorporate details of the crystallographic microstructure of martensite into thermodynamic formulations, micromechanical constitutive models take transformation strains of martensitic variants into account by the crystallographic theory of the martensitic transformation [33–35] or the geometrically nonlinear theory of martensite [24, 27] in the constitutive framework. Some micromechanical models went further to consider self-accommodation, reorientation and detwinning, and other features of martensitic transformation [36–40]. Micromechanical models have proven instrumental for modeling the material response under multi-axial stress states. Several authors obtained accurate predictions of macroscopic mechanical behavior of SMAs [28, 41–47]. However, there have been far fewer continuum models for SMCs and efforts have largely gone into the development of atomistic or phase field models. A comprehensive review of computational models for SMCs can be found in [48]. Zhang and Zaem conducted extensive molecular dynamics (MD) studies of various aspects of inelastic deformation of single crystalline yttria-stabilized tetragonal zirconia (YSTZ) nanopillars including different deformation mechanisms, orientation dependency, grain size dependency, and the influence of pre-existing defects [49–52]. Phase field models have also been shown to be powerful tools in modeling martensitic transformation in SMAs [53–55] and, more recently, SMCs [56–58]. Various types of phase field models have been developed for tetragonal to

monoclinic transformation where different thermodynamic potentials and order parameters are used. In particular, in [57] a three-dimensional phase field model for tetragonal-to-monoclinic transformation in zirconia was proposed. The model took into account all possible martensite variants from different correspondences and was used to study the formation of a monoclinic embryo in a tetragonal single crystal. This model successfully captured the variant selection process based on the minimum formation energy and the effect of variant strain accommodation during the tetragonal-to-monoclinic transformation. It also reproduced the microstructural patterns observed in experiments. In [58], the authors combined a variational formulation of crack propagation with a two-dimensional phase field model of tetragonal-to-monoclinic transformation. The model was employed to study crack growth in a single-crystal tetragonal zirconia.

In this work, we implemented a numerical framework for modeling martensitic transformation in zirconia-based SMCs at the continuum level incorporating micromechanical information. The anisotropic rate-dependent constitutive model is based on the three-dimensional constitutive framework for single-crystal SMAs developed in [29–31, 39]. We extended the framework to SMCs and used the geometrically nonlinear theory of martensite to identify the particular 24 transformation systems in zirconia-based SMCs, based on the knowledge of lattice parameters. In addition, we extended the modeling framework to account for the non-Schmid effect observed in SMCs [3], which to our knowledge has never been done to any prior FEM-based SMC model. The model was calibrated against micro-pillar compression tests presented in [3, 4], and subsequently used to verify the orientation dependence of transformation stress and strain. The model was incorporated in our in-house computational framework Σ MIT to perform large-scale finite element simulations [59–61]. We then conducted high-resolution three-dimensional finite element simulations to explore and understand strain incompatibilities at grain boundaries due to both elastic and transformation anisotropy in bi-crystals SMCs with general misorientations. The organization of this paper is as follows. In Sect. 2, we described the computational framework including the single-crystal constitutive formulation and update algorithm. In Sect. 3, we calibrated the model using experimental data

obtained by micro-compression tests. In Sect. 4, we conducted a series of finite element simulations to investigate different types of strain incompatibilities arising at grain boundaries in zirconia using the calibrated model, followed by analysis and discussion of the results. Conclusions and contributions of this paper are presented in Sect. 5.

Micromechanics-based model

The proposed constitutive model for single-crystal zirconia-based SMCs is built upon the general continuum framework for describing martensitic transformations at the single-crystal level proposed by Anand et al [29–31, 39]. This framework requires the identification and geometric description of the transformation systems pertaining to the specific crystal structure of the material. The geometric characteristics of the transformation systems for martensitic transformations are defined by the normal to the austenite–martensite interface plane (habit plane), \mathbf{m}_0^i , and the transformation strain direction vector \mathbf{b}_0^i , where i is the index of the existing transformation systems. These quantities can be computed from the geometrically nonlinear theory of martensite [24–27] based on the crystal structure of the austenite and martensite phases of the material and the lattice parameters in both phases. Simha [25] used this theory to compute the transformation systems in zirconia where the phases are respectively tetragonal and monoclinic for a particular set of lattice parameters, see also [26] for a review of martensitic transformation systems in other ceramics. Here, we computed the transformation systems for the specific composition of the ceria-doped zirconia used in the experiments from [3]. A summary of the approach and resulting 24 systems is shown in the Appendix (Table 1).

Importantly, the martensitic transformation in zirconia not only involves lattice shear as in many metallic shape memory materials, but it is also accompanied by a significant volume change ($\sim 4\%$) [8]. From a micromechanics perspective, transformation systems in zirconia are non-orthogonal and this results in a non-Schmid effect during the transformation. In order to take into account the normal deformation in each transformation system which is responsible for the volume change, we adapted the

Table 1 Habit plane normal and transformation directions of the 24 transformation systems. The monoclinic lattice parameters are $a = 0.51597, b = 0.52222, c = 0.53227, \beta = 99.14$

i	$[m^i]_1$	$[m^i]_2$	$[m^i]_3$	$[b]_1$	$[b^i]_2$	$[b^i]_3$
1	0.8230	-0.2522	-0.5090	0.0265	-0.0081	0.0169
2	-0.8230	0.2522	-0.5090	-0.0265	0.0081	0.0169
3	0.8230	0.2522	-0.5090	0.0265	0.0081	0.0169
4	-0.8230	-0.2522	-0.5090	-0.0265	-0.0081	0.0169
5	0.7856	-0.3519	-0.5090	0.0253	-0.0113	0.0169
6	-0.7856	0.3519	-0.5090	-0.0253	0.0113	0.0169
7	0.6987	0.5027	-0.5090	0.0225	0.0162	0.0169
8	-0.6987	-0.5027	-0.5090	-0.0225	-0.0162	0.0169
9	0.5027	-0.6987	-0.5090	0.0162	-0.0225	0.0169
10	-0.5027	0.6987	-0.5090	-0.0162	0.0225	0.0169
11	-0.3519	-0.7856	-0.5090	-0.0113	-0.0253	0.0169
12	0.3519	0.7856	-0.5090	0.0113	0.0253	0.0169
13	0.7856	0.3519	-0.5090	0.0253	0.0113	0.0169
14	-0.7856	-0.3519	-0.5090	-0.0253	-0.0113	0.0169
15	0.6987	-0.5027	-0.5090	0.0225	-0.0162	0.0169
16	-0.6987	0.5027	-0.5090	-0.0225	0.0162	0.0169
17	0.7856	0.3519	-0.5090	0.0162	0.0225	0.0169
18	-0.7856	-0.3519	-0.5090	-0.0162	-0.0225	0.0169
19	0.6987	-0.5027	-0.5090	-0.0113	0.0253	0.0169
20	-0.6987	0.5027	-0.5090	0.0113	-0.0253	0.0169
21	0.2522	0.8230	-0.5090	0.0081	0.0265	0.0169
22	-0.2522	-0.8230	-0.5090	-0.0081	-0.0265	0.0169
23	-0.2522	0.8230	-0.5090	-0.0081	0.0265	0.0169
24	0.2522	-0.8230	-0.5090	0.0081	-0.0265	0.0169

formulation in [62] developed for crystalline silicon. A robust explicit algorithm is developed to update the constitutive law. The formulation of the constitutive model follows closely the presentation in [31]. For completeness, the main steps in the formulation are summarized below.

Kinematics

A multiplicative decomposition of the deformation gradient into elastic and inelastic components is assumed,¹

$$\mathbf{F} = \mathbf{F}^e \mathbf{F}^p \quad (1)$$

¹ \mathbf{F}^p is not the plastic part of the deformation gradient as is normally used in the plasticity theory and the subscript p is for phase transformation.

Free energy

The free energy per unit reference volume ψ is decomposed into three terms: the strain energy ψ^e , the energy of phase transformation ψ^p , and the thermal energy ψ^θ [63]:

$$\psi(\mathbf{E}^e, \theta, \xi) = \psi^e(\mathbf{E}^e, \theta, \xi) + \psi^p(\xi, \theta) + \psi^\theta(\theta) \quad (2)$$

where ξ is the martensite volume fraction, and θ is the temperature.

The strain energy is given by:

$$\psi^e(\mathbf{E}^e, \theta, \xi) = \frac{1}{2} \mathbf{E}^e \cdot \mathcal{C}(\xi) \mathbf{E}^e \quad (3)$$

where \mathcal{C} is the fourth-order elasticity tensor. Note that in this study we neglected the thermal expansion term. The second Piola–Kirchhoff elastic stress tensor \mathbf{T}^e follows from this expression as:

$$\mathbf{T}^e = \frac{\partial \psi^e}{\partial \mathbf{E}^e} = \mathcal{C} \mathbf{E}^e \tag{4}$$

The elastic moduli \mathcal{C} are obtained in terms of the respective values for the austenite and martensite phases C_{ijkl}^a and C_{ijkl}^m , as a function of the martensite volume fraction ξ using the rule of mixtures,

$$C_{ijkl} = \xi C_{ijkl}^m + (1 - \xi) C_{ijkl}^a \tag{5}$$

\mathbf{T}^e is related to the first Piola–Kirchhoff stress \mathbf{S} and Cauchy stress σ through:

$$\mathbf{S} = \mathbf{F}^e \mathbf{T}^e \mathbf{F}^{eT} \tag{6}$$

$$\sigma = J^{-1} \mathbf{F}^e \mathbf{T}^e \mathbf{F}^{eT} \tag{7}$$

The energy of phase transformation is given by,

$$\psi^p(\xi, \theta) = \frac{\lambda_T}{\theta_T} (\theta - \theta_T) \xi + \frac{1}{2} \sum_{i,j} g^{ij} \xi^i \xi^j \tag{8}$$

where $\theta_T \equiv \frac{1}{2}(\theta_{ms} + \theta_{as})$ is the phase equilibrium temperature, λ_T is the latent heat of phase transformation at θ_T , and g^{ij} is the interaction matrix that accounts for possible energetic interactions between transformation systems. Here we shall neglect the interactions between systems and consider $g^{ij} = 0$ in our application of the theory to zirconia due to the lack of experimental data that would allow us to calibrate the interaction coefficients.

The thermal energy is given by,

$$\psi^\theta(\theta) = c(\theta - \theta_0) - c\theta \ln \frac{\theta}{\theta_0} \tag{9}$$

where c is the constant specific heat, and θ_0 is the reference temperature.

Transformation conditions

Similar to the crystal plasticity theory [64], a resolved shear stress for phase transformation in each transformation system is defined as follows,

$$\tau^i = \mathbf{b}_0^i \cdot (\mathbf{C}^e \mathbf{T}^e) \mathbf{m}_0^i \tag{10}$$

A thermodynamic force b (back stress) that is work conjugate to the martensite volume fraction ξ is defined as,

$$b = \frac{\partial \psi^p}{\partial \xi} = \frac{\lambda_T}{\theta_T} (\theta - \theta_T) \tag{11}$$

For simplicity, we assume b remains the same for all transformation systems. Neglecting the interaction

effects of different systems, the driving force f^i for phase transformation is defined as,

$$f^i = \tau^i - b \tag{12}$$

Forward and reverse transformation can only occur when the driving force f^i in the transformation system reaches a critical value Y^i . The transformation criteria are as follows [31],

$$f^i(\dot{\xi}) = \begin{cases} Y_+^i & \text{for } \dot{\xi}^i > 0, \\ -Y_-^i & \text{for } \dot{\xi}^i < 0. \end{cases} \tag{13}$$

where Y_+^i and Y_-^i are material parameters defined as the critical transformation resistance for forward and reverse transformation, respectively.

The consistency condition for phase transformation in each system can be obtained in a similar manner [29] to that in the plasticity theory [64],

$$\overline{(\tau^i - b - Y_+^i)}_{\dot{\xi}^i} = 0 \quad \text{or} \quad \overline{(\tau^i - b + Y_-^i)}_{\dot{\xi}^i} = 0 \tag{14}$$

Rate-dependent theory

The rate-independent formulation requires an implicit algorithm to determine the active transformation systems and associated martensite volume fractions. This is usually fraught with numerical difficulties which stem from the lack of convexity of the problem. A rate-dependent transformation condition [31], facilitates the use of an explicit algorithm, which robustly produces acceptable numerical results [65, 66]. Such a rate-dependent flow rule will reduce to the rate-independent one (Eq. 14) in the limit where the rate-dependent constant approaches zero. Closely following the derivation in [31], the main steps in the formulation are summarized below,

$$\tau^i - b = \begin{cases} +|\frac{\dot{\xi}^i}{\xi^i}|^m Y_+^i & \text{for } \dot{\xi}^i \geq 0, \\ -|\frac{\dot{\xi}^i}{\xi^i}|^m Y_-^i & \text{for } \dot{\xi}^i \leq 0, \end{cases} \tag{15}$$

where the reference transformation rate $\frac{\dot{\xi}^i}{\xi^i}$, and the rate-dependent constant m , are additional material parameters for the rate-dependent model.

The transformation condition in the rate-dependent theory can be obtained by inverting Eq. 15,

$$\dot{\xi}^i = \begin{cases} +\bar{\xi}^i \left| \frac{\tau^i - b}{Y_+^i} \right|^{1/m} & \text{for } \tau^i - b \geq 0, \\ -\bar{\xi}^i \left| \frac{\tau^i - b}{Y_-^i} \right|^{1/m} & \text{for } \tau^i - b \leq 0, \end{cases} \quad (16)$$

Equation 16 shows that the rate of change in martensite volume fraction in each transformation system $\dot{\xi}^i$ can be obtained in a straightforward manner in the rate-dependent theory. The volume fraction of martensite ξ^i is updated at each time step upon solving for $\dot{\xi}^i$. Closely following the framework in [29, 31], we assume the critical transformation stress remains the same for all transformation systems, $Y_+^i = Y_-^i = Y$ for simplicity and lacking better experimental evidence.

Phase transformation flow rule

As stated before, the martensitic transformation in zirconia is accompanied by a significant volume change and stresses normal to the habit plane also contribute to the driving force for martensitic transformation in addition to shear stresses. From a micromechanics perspective, this is explained by the fact that transformation systems in zirconia are non-orthogonal which introduces a non-Schmid effect in the transformation response. In order to account for this non-Schmid effect, we adapted the formulation in [62] to include the normal deformation during transformation.

The direction of phase transformation \mathbf{b}_0 is decomposed as,

$$\xi \mathbf{b}_0 = \zeta_s \mathbf{s}_0 + \zeta_n \mathbf{m}_0 \quad (17)$$

where \mathbf{s}_0 and \mathbf{m}_0 are the shear and normal directions, respectively, and $\zeta_n = \zeta \mathbf{b}_0 \cdot \mathbf{m}_0$.

By including the normal deformation across the habit plane, the transformation velocity gradient becomes,

$$\mathbf{L}^p = \sum_{i=1}^N \frac{\dot{\xi}^i}{1 + \xi^i} \mathbf{b}_0^i \otimes \mathbf{m}_0^i \quad (18)$$

In summary, the rate-dependent flow rule of the phase transformation reads,

$$\begin{aligned} \dot{\mathbf{F}}^p &= \mathbf{L}^p \mathbf{F}^p \\ \mathbf{L}^p &= \sum_{i=1}^N \frac{\dot{\xi}^i}{1 + \xi_n^i} \mathbf{b}_0^i \otimes \mathbf{m}_0^i \\ \dot{\xi}^i &= \bar{\xi}^i \left| \frac{\tau^i - b^i}{Y} \right|^{1/m} \text{sgn}(\tau^i - b^i) \end{aligned} \quad (19)$$

Summary of governing and constitutive equations

The linear momentum balance:

$$\text{Div } \mathbf{S} + \mathbf{b} = \rho_0 \ddot{\phi} \quad (20)$$

The elastic stress–strain relation:

$$\mathbf{T}^e = \mathcal{C}[\mathbf{E}^e - \mathbf{A}(\theta - \theta_T)] \quad (21)$$

The transformation back stress:

$$b = \frac{\partial \psi^p}{\partial \xi} = \frac{\lambda_T}{\theta_T} (\theta - \theta_T) \quad (22)$$

The resolved shear stress for each transformation system:

$$\tau^i = \mathbf{b}_0^i \cdot (\mathbf{C}^e \mathbf{T}^e) \mathbf{m}_0^i \quad (23)$$

The rate-dependent phase transformation flow rule:

$$\begin{aligned} \dot{\mathbf{F}}^p &= \mathbf{L}^p \mathbf{F}^p, \\ \mathbf{L}^p &= \sum_{i=1}^N \frac{\dot{\xi}^i}{1 + \xi_n^i} \mathbf{b}_0^i \otimes \mathbf{m}_0^i \\ \dot{\xi}^i &= \bar{\xi}^i \left| \frac{\tau^i - b}{Y} \right|^{1/m} \text{sgn}(\tau^i - b), \end{aligned} \quad (24)$$

It bears emphasis that the use of the constitutive model in calculations requires the specification of the constitutive model parameters: anisotropic elastic moduli in both phases C_{ijkl}^a, C_{ijkl}^m , the transformation stress Y , the back stress b , and the orientation of each crystal relative to the frame of the simulations in which the loading directions are specified. In our implementation of the model, we use the rotation matrix to define the crystal orientation with respect to the global reference frame. This rotation matrix is used to effect the necessary tensorial transformations to the global coordinate system in which the loading is applied. The rotation matrix can also be obtained from the Euler angles determined experimentally.

Explicit constitutive update algorithm

An explicit algorithm that solves for the volume fraction of martensite in each transformation system in a sequential manner is implemented for updating the constitutive equations [65, 66]. Each transformation system is handled iteratively in such a calculation. The determination of forward or reverse transformation is distinguished by the sign of the overstress, where positive values indicate forward transformation (to monoclinic martensite) and negative ones a reverse transformation (to tetragonal austenite). At each time step, the transformation system with largest absolute overstress $|\tau^i - b|$ is identified and the corresponding volume fraction is updated according to Eq. 16. The computation proceeds with the other systems in decreasing order of absolute overstress until there is no inactive system with admissible overstress (i.e., for the forward transformation the resolved shear stress exceeds the back stress, and for the reverse transformation the resolved shear stress is smaller than the back stress). The detailed algorithm is as follows,

1. Calculate the volume fraction ζ^i for all systems based on the step t_n ;
2. Compute $\mathbf{F}^e = \mathbf{F}_{n+1} \mathbf{F}_n^{p-1}$ and evaluate τ^i for all systems;
3. Calculate the overstress $\tau^i - b$ for all systems and determine its largest absolute value. If this overstress is negative: if $\tau^i - b > 0$ for all systems, go to step 6; if this overstress is positive: if $\tau^i - b < 0$ for all systems, go to step 6. Otherwise:
4. Evaluate $\Delta \mathbf{F}^p = \frac{\zeta_n^i}{1 + \zeta_n^i} dt (\mathbf{b}_0^i \otimes \mathbf{m}_0^i)$ based on the system i with the largest absolute value of overstress;
5. Premultiply \mathbf{F}^p by $\Delta \mathbf{F}^p$, return to step 2 using the updated \mathbf{F}^p ;
6. Compute new volume fraction rates $\dot{\zeta}^i$ for each transformation system.

Model calibration using nano-pillar compression tests

The constitutive model described above is calibrated against the micro-pillar compression tests in [3, 4], where grain orientations of single-crystal micro-pillar samples were identified using electron backscatter

diffraction and correlated with room temperature mechanical response. 24 transformation systems are identified from correspondence B. (Neither correspondence A or C produces any habit plane for this specific set of lattice parameters.) These experiments provide the following data: the critical stress for room temperature transformation, the transformation strain that results, and an approximate value for the loading (tetragonal) elastic modulus. A wide variety of mechanical responses was observed amongst differently oriented samples, including martensitic transformation without cracking, plastic slip, and fracture. An important limitation of micro-pillar compression experiments is the significant difference between the measured and theoretical loading modulus [4]. In this particular reference, it was observed that for most of the samples with smaller transformation stresses, micro-compression experiments underestimated elastic moduli significantly. This discrepancy was attributed to several aspects of the micro-compression experiments such as substrate and tip compliance, minor misalignments, possible defects in the micro-pillar samples and indentation compliance at the point of contact of the tip and pillar.

We conducted simulations of zirconia micro-pillars with various orientations undergoing compression. In the simulation, we assumed an idealized compression test and artificial compliance was not considered. We therefore expect to obtain a much stiffer elastic response than the experiments. A test of a micro-pillar with Euler angles $E1 = 53^\circ$, $E2 = 122^\circ$, $E3 = 299^\circ$ that underwent full martensitic transformation without cracking was taken as the basis for calibrating the model parameters.

Elastic constants for both austenite and martensite phases were obtained from [67]. Figure 1a shows the results of the model using the theoretical values of the elastic constants, where the transformation stress $Y = 6$ MPa and backstress $b = 3$ MPa are calibrated to match the experimental results. In this particular orientation, the elastic loading modulus in the experiment was about three times smaller than the theoretical value, as a result of the machine compliance issues described above. Accordingly, in Fig. 1b we perform an a posteriori linear machine compliance correction of the strain, to force a match with the theoretical modulus of the tetragonal phase at zero strain. Since the loading and unloading moduli are similar, we used the value obtained from the

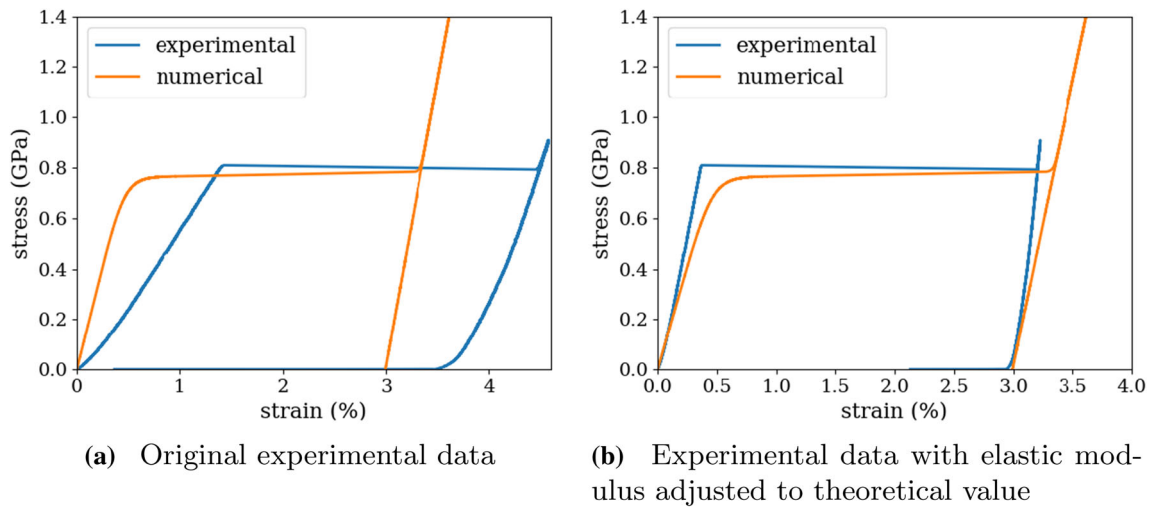


Figure 1 Simulation results compared with experiments, Euler angles = [53, 122, 299].

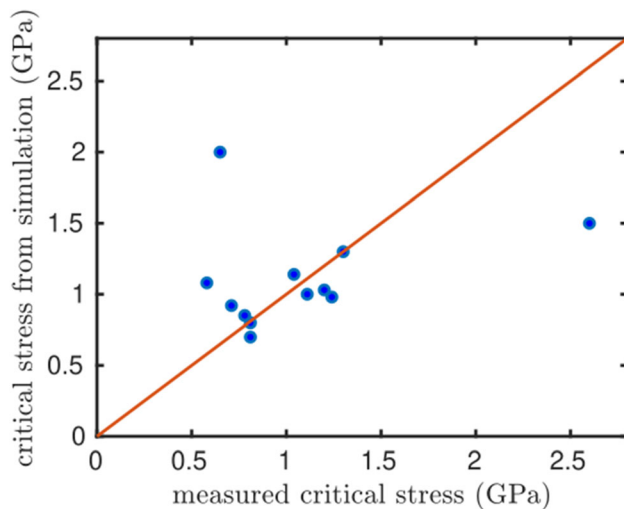


Figure 2 Orientation dependence of critical transformation stress: simulation results compared with experiments.

austenite phase for both loading and unloading cases for simplicity. Figure 1b shows that after adjusting the moduli to the theoretical value, the model captures the stress–strain response of the test using the calibrated parameters quite well.

To verify the ability of the calibrated model to capture the orientation dependence of transformation stress in zirconia, we conducted simulations using various orientations of the samples tested in [4] that underwent martensitic transformation without fracture. As a way of summarizing the results, we

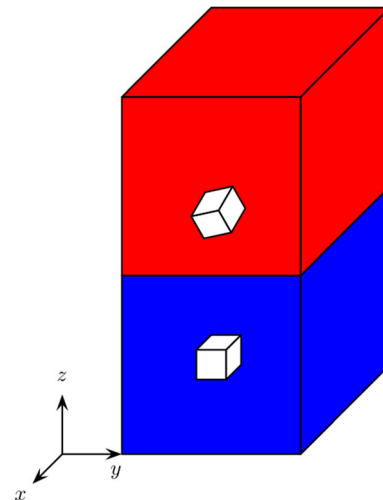


Figure 3 An example of the bi-crystal specimen.

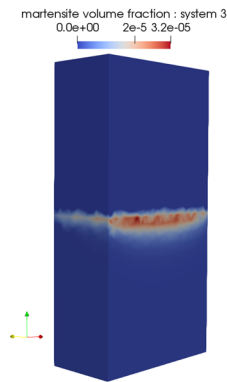
extracted from the simulation results the calculated transformation stresses for each orientation and compared them with the experimentally measured values in Fig. 2. The results show that, except for a few outliers, the theoretical predictions are a reasonable match to the measured values, despite the unquantified uncertainties, including those in the measurements of grain orientation, possible defects in the micro-pillars, the control of boundary conditions and shape of the micro-pillars.



(a) Von Mises stress at a bi-crystal cross section plane parallel to $x - z$ plane when $\epsilon = 0.6\%$ (b) Von Mises stress at a bi-crystal cross section plane parallel to $x - y$ plane when $\epsilon = 0.6\%$



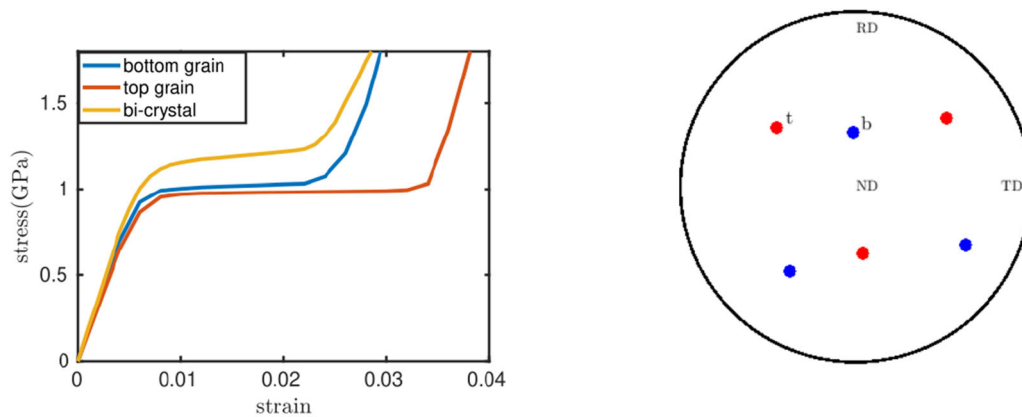
(c) Corresponding total martensite volume fraction (d) Corresponding martensite volume fraction in system 19



(e) Corresponding martensite volume fraction in system 3

Figure 4 Contours of: **a** von Mises; **c–e** martensite volume fraction; in the bi-crystal cross section with normal y ; **b** von Mises in the bi-crystal cross section with normal z . The figures illustrate that there is a strong stress concentration near the bi-crystal

interface at a low strain level. Figures **b–d** show at that level, there is an incipient but very low transformation. Martensitic transformation is primarily triggered in system 19, but the overall amount of martensite volume fraction is still very small.



(a) Maximum von Mises stress at the grain boundary plane in bi-crystal and (b) Pole figure showing the $[001]$ $[010]$ $[110]$ poles of the top (red, with the long axis labeled as 't') and bottom grain (blue, with the long axis labeled as 'b')

Figure 5 Case 1: Grain boundary configuration with high elastic incompatibility.

Competition between phase transformation and incompatibility at grain boundaries in bi-crystals

To improve our understanding of incompatibilities arising from elastic anisotropy as well as incompatibility of transformations at grain interfaces, high-resolution three-dimensional finite element simulations of bi-crystal zirconia specimens subjected to compressive loading were conducted. We considered a simple scenario in which two cubic grains were stacked along the z axis. The grain boundary plane was oriented parallel to the $x-y$ plane and the loading direction is along the z -axis. Figure 3 illustrates the geometry of the bi-crystal specimen. Unit cells in each grain demonstrate different orientations of the top and bottom grain.

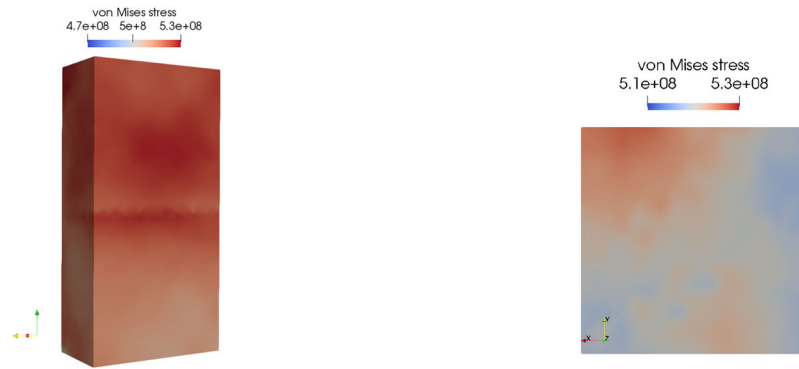
We first sampled misorientation space to explore different types of grain boundary incompatibilities. We selected orientations from the experiments in [4] that exhibited martensitic transformation under compression, and avoided orientations that slipped or fractured in the single-crystal tests. We started by fixing the orientation of the bottom grain ($E1=3^\circ$, $E2=146^\circ$, $E3=306^\circ$) and considered two different orientations for the top grain which resulted in distinct strain incompatibility types.

We ran simulations up to 5% strain which exceeds the transformation strain for the single-crystal orientations tested here, and monitored the evolution of

the von Mises equivalent stress at the grain boundary as the deformation progresses. The von Mises stress provides a metric for quantifying the magnitude of the complex deviatoric stress state at the grain boundary. We also monitored the volume fraction of martensite in each transformation system and overall to understand the onset and progression of the transformation at the grain boundary versus the bulk of the grain. To understand the influence of grain boundaries on the stress field, we conducted corresponding simulations on single crystals with the same orientations as each individual grain in the bi-crystal.

We considered two different cases which, as we shall see, result in two distinct types of incompatibility. In Case 1, the top grain orientation is given by Euler angles $E1=53^\circ$, $E2=122^\circ$, $E3=299^\circ$, whereas in Case 2, the Euler angles for the top grain are $E1=84^\circ$, $E2=142^\circ$, $E3=118^\circ$. The results of the two simulations are shown in Figs. 4, 5, 6, 7.

Figure 4a, b, and c, respectively, shows snapshots of the von Mises stress at different cross sections, and the total martensite volume fraction at the bi-crystal grain boundary obtained in Case 1 at a small strain level of 0.6%, at which point the deformation is still ostensibly elastic with martensite volume fraction on the order of 10^{-2} . As can be observed, there is a significant amount of stress concentration at the grain boundary plane in the bi-crystal, despite there being almost no transformation. The maximum von Mises



(a) Von Mises stress at a bi-crystal cross section parallel to $x - z$ plane at $\epsilon = 0.3\%$ (b) Von Mises stress at a bi-crystal cross section parallel to $x - y$ plane at $\epsilon = 0.3\%$



(c) Corresponding total martensite volume fraction at $\epsilon = 0.3\%$ (d) Von Mises stress at a bi-crystal cross section parallel to $x - z$ plane at $\epsilon = 2\%$



(e) Von Mises stress at a bi-crystal cross section parallel to $x - y$ plane at $\epsilon = 2\%$ (f) Corresponding total martensite volume fraction at $\epsilon = 2\%$

Figure 6 Contours of: **a** von Mises; **c** martensite volume fraction in the bi-crystal cross section with normal y ; **b** von Mises in the bi-crystal cross section with normal z at $\epsilon = 0.3\%$; **d** von Mises; **f–j** martensite volume fraction in the bi-crystal cross-section with normal y ; **e** von Mises in the bi-crystal cross-section with normal z at $\epsilon = 2\%$. Figures **a–c** illustrate that there is no significant

stress concentration near the bi-crystal interface at this strain level. Figures **d–j** show that at a higher strain level, the bottom crystal has almost fully transformed and there is a strong stress concentration near the bi-crystal grain boundary. System 19 is the most favorably oriented system for transformation.



(g) Martensite volume fraction in system 2 at $\epsilon = 2\%$ (h) Martensite volume fraction in system 12 at $\epsilon = 2\%$



(i) Martensite volume fraction in system 14 at $\epsilon = 2\%$ (j) Martensite volume fraction in system 19 at $\epsilon = 2\%$

Figure 6 continued.

stress can be seen near grain boundary (≈ 0.96 GPa). Figure 4c–e shows the total volume fraction as well as the volume fraction in selected transformation systems (3 and 19). Though the overall martensitic volume fraction is extremely small, it is still worth mentioning that the main contribution of martensitic transformation came from system 19, which in this case is the most favorably oriented for transformation, i.e., where the resolved shear stress is the largest. In contrast, system 3 is an example of a system where transformation has not yet been triggered and the volume fraction is 3 orders of magnitude smaller than that in system 19. Figure 5a shows the comparison of the von Mises stress in the single crystals and the maximum value in the bi-crystal grain boundary as a function of strain for Case 1. As may be noted, the von Mises stress at the grain boundary plane grows significantly larger than that in either single-crystal before the occurrence of phase transformation.

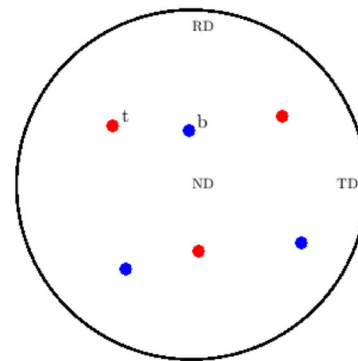
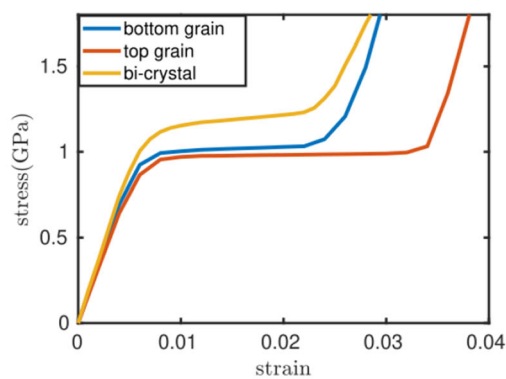
These results suggest that the source of strain incompatibility is elastic anisotropy.

Figures 6 and 7 show the corresponding results for Case 2. Figures 6a, b and c show the von Mises stress at different bi-crystal cross sections and corresponding martensitic volume fraction when $\epsilon = 0.3\%$. At this strain level, the stress concentration at the grain boundary plane is extremely low and there is no transformation. (Total volume fraction is on the order of 10^{-4} .) This grain boundary configuration therefore has insignificant elastic incompatibility. Figure 6d–j show the corresponding results at $\epsilon = 2\%$, as well as martensite volume fraction in several transformation systems. There is a significant stress concentration at the grain boundary plane at this strain level, as the maximum von Mises stress at the grain boundary is about 1.3 GPa, which is about 1.44 times larger than that in the regions that are farther from grain boundary. As shown in Fig. 6e, the corresponding

martensitic volume fraction in the bottom grain at this strain level is about 1 except for the region near grain boundary, which indicates that the bottom grain has fully transformed to martensitic phase except for the region near grain boundary. The top grain has also seen a significant amount of transformation with the volume fraction ranging from 0.38 to 0.6, which suggests that stress concentrations are due to the incompatibility of the anisotropic transformation strain at the grain boundary instead of elastic anisotropy at this level of deformation. It is also worth mentioning that martensitic volume fraction in system 19 is 3–4 orders of magnitude larger than that in other systems, which makes it the dominant transformation system as it contributes the most to the total volume fraction. As shown in Fig. 7a, there is a very low level of elastic incompatibility in the austenite phase, as the three initial slopes coincide. As a result, the maximum von Mises stress at the grain boundary plane remains similar to that in the single crystal. However, as transformation progresses, the maximum von Mises stress at the bi-crystal interface grows much larger than inside either single crystal. At strain level $\epsilon = 2\%$, the stress concentration factor at the grain boundary is about 1.6. The maximum von Mises stress at the grain boundary grows from 1 to 1.3 GPa during transformation, while von Mises stresses in the two single-crystal cases plateau at 0.7 GPa and 1 GPa, respectively. This

suggests that the source of stress concentration is the incompatibility of the transformation strains. Specifically, at the grain interface, the transformation strain on one grain cannot be accommodated by that in the neighboring grain due to the anisotropic nature of the martensitic transformation, and the deformation constraints lead to stress concentration. These figures suggest that a possible way to quantify the level of elastic incompatibility is to compare the growth of the von Mises stress at the grain boundary relative to the single-crystal response during the elastic range. Similarly, one way to quantify the transformation incompatibility is to compare the von Mises stress at the grain boundary relative to the single-crystal response at a certain strain level during transformation.

Having established the two basic types of sources of incompatibilities, we next conducted a series of simulations with 43 different orientations of the top grain with the orientation of the bottom grain fixed. The grain misorientations are presented in a pole figure in the Appendix (Fig. 8). We used the ratio of the initial rate of growth of the von Mises stress at the bi-crystal grain boundary relative to the single-crystal response of the bottom grain as a measure of the grain boundary stiffness induced by elastic incompatibility. Similarly, we used the ratio of the von Mises stress at the bi-crystal grain boundary at 2.2% strain (stress concentration factor), relative to the



(a) Maximum von Mises stress at the grain boundary plane in bi-crystal and single crystals (b) Pole figure showing the [001] [010] [110] poles of the top (red, with the long axis labeled as 't') and bottom grain (blue, with the long axis labeled as 'b')

Figure 7 Grain boundary configuration with low elastic incompatibility.

single-crystal response of the bottom grain to measure transformation incompatibility.

Figure 9a shows the grain boundary stiffness ratios in 43 bi-crystal specimens and their disorientation angles. Each point represents a bi-crystal with a disorientation angle defined as the minimum rotation angle with the misorientation axis located in the Standard Stereographic Triangle. As indicated in Fig. 9a, among these bi-crystals with various misorientations, the largest stiffness ratio is slightly below 1.2, suggesting that in general elastic incompatibility in this zirconia-based SMC is rather low. One can also notice that there is a clear correlation between disorientation angles and elastic incompatibilities. Most bi-crystal specimens with smaller disorientation angles are shown to have small stiffness ratios. By contrast, when the disorientation angle is larger, elastic incompatibility is higher which results in larger stress concentrations in the elastic range. It is worth noting that the two bi-crystals with smallest disorientation angles appear to be outliers with much larger incompatibilities from elasticity than those with disorientation angles between 30° and 50° .

Figure 9b shows the respective results of maximum von Mises stress concentration factor at the grain boundary plane at 2.2% strain. Among the 43 bi-crystals, the largest von Mises stress concentration

factor is 3.1 and it occurs in the bi-crystal with a disorientation angle about 70° . As demonstrated in Fig. 9b, bi-crystals with larger von Mises stress and therefore higher transformation incompatibility often correspond to larger disorientation angles, with some outliers in the results especially for samples with small orientation angles. The outliers could be due to the inaccuracy in identifying the grain orientation of the samples. Another possible explanation for the outliers is that the correlation between disorientation angles and stress concentration factors is more evident in samples with large orientation angles, yet the correlation is not very clear for samples with smaller disorientation angles. These results also suggest that elastic incompatibility in zirconia may be lower in magnitude relative to incompatibilities resulting from transformation.

Conclusion

We have conducted a simulation study attempting to characterize the sources and magnitude of strain incompatibility at bi-crystal interfaces in SMCs. To this end, we have implemented a micromechanics-based model for SMCs incorporating both elastic and transformation anisotropy at the grain level. We incorporated the non-Schmid effect into the model to account for the volume changes during martensitic transformation which is a unique feature for zirconia-based SMCs. The model was calibrated against micro-compression tests conducted in [3, 4] and shown to capture the orientation dependence of transformation fairly accurately. Three-dimensional finite element simulations using the micromechanical model enabled the investigation of the evolution of stress concentrations at the grain boundary due to either elastic or transformation strain incompatibility, as well as the analysis of the evolution of the martensite volume fraction, which has not been addressed in SMCs before. The level of stress concentration at the grain boundary as measured by the maximum von Mises stress strongly depends on the crystal boundary misorientation. Large elastic anisotropy leads to severe deformation incompatibility and high von Mises stress concentration at the grain boundary at relatively low strains. We identified two particular cases with distinct stress–strain responses and found that when the crystals are elastically compatible, high stress concentrations at the grain

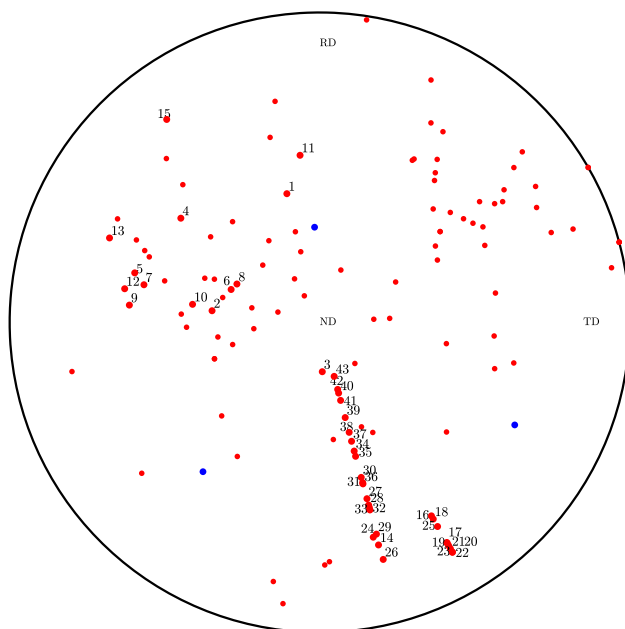
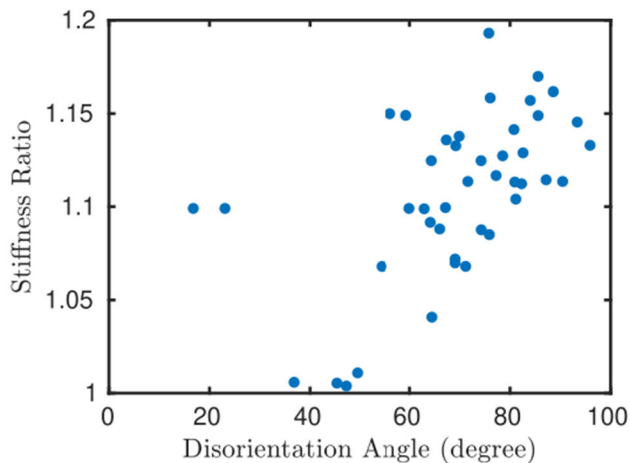
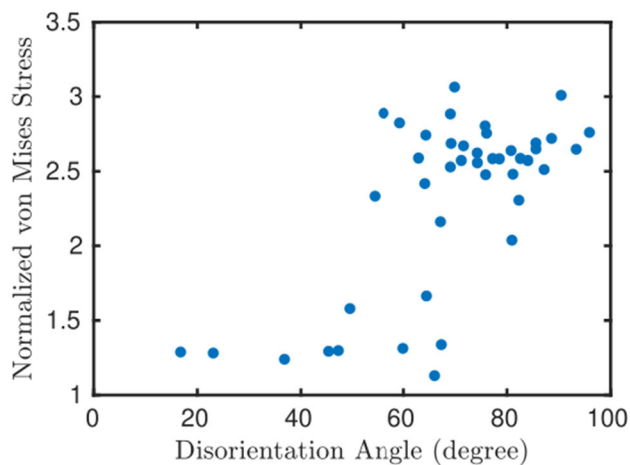


Figure 8 A pole figure showing the [100], [010], [001] crystal directions of the bottom (blue) and top grain (red) of 43 bi-crystals studied in the simulations with the long axis [001] pole labeled.



(a) Grain boundary stiffness ratio



(b) Normalized maximum von Mises stress at 2.2% strain level

Figure 9 Quantitative indicators of elastic and transformation incompatibility at bi-crystal grain boundary vs. disorientation angles (bottom grain [3, 146, 306]).

boundary, and therefore transformation strain incompatibilities are still possible due to the anisotropic nature of the martensitic transformation. We then conducted a series of simulations over the misorientation space, in search of grain boundary configurations that can achieve the full ductility potential of the single crystal. We analyzed the relationship between different types of incompatibilities and grain boundary characteristics, and the results indicate a strong correlation between both types of strain incompatibilities and the disorientation angle. This approach could be used to identify misorientations that reduce or minimize elastic and

transformation incompatibility, thus extending the superelastic range of SMCs to potentially achieve the ductility limits of single crystals.

Acknowledgements

The authors gratefully acknowledge support from the U.S. Army through the Institute for Soldier Nanotechnologies under Contract ARO69680-18 with the U.S. Army Research Office.

Funding

Open Access funding provided by the MIT Libraries.

Declarations

Conflict of interest The authors declare that they have no known competing financial interests or personal relationships that could have appeared to influence the work reported in this paper.

Open Access This article is licensed under a Creative Commons Attribution 4.0 International License, which permits use, sharing, adaptation, distribution and reproduction in any medium or format, as long as you give appropriate credit to the original author(s) and the source, provide a link to the Creative Commons licence, and indicate if changes were made. The images or other third party material in this article are included in the article's Creative Commons licence, unless indicated otherwise in a credit line to the material. If material is not included in the article's Creative Commons licence and your intended use is not permitted by statutory regulation or exceeds the permitted use, you will need to obtain permission directly from the copyright holder. To view a copy of this licence, visit <http://creativecommons.org/licenses/by/4.0/>.

Appendix

Habit plane normal and transformation directions of the 24 transformation systems used in the model

Given the lattice parameters and symmetry of the austenite and martensite phases, we applied the

nonlinear theory of martensite to obtain the transformation systems for zirconia [25]. The calculation requires the knowledge of the mapping from the austenite configuration to the martensite one, which can be obtained by constructing the deformation gradient that takes a unit cell in the austenite phase to martensite. From there one then obtains the stretch tensor \mathbf{U}_0 , as well as all possible variants of martensite by applying rotations to the \mathbf{U}_0 . Then one can obtain the transformation systems by solving the twinning and habit plane equations. The algorithm is summarized as follows:

1. Construct Bain strains \mathbf{U}_0 (a mapping from the austenite point group \mathcal{P}_a to the martensite point group \mathcal{P}_m) for the tetragonal to monoclinic transformation in zirconia;
2. Calculate all the possible variants of martensite $\mathbf{U}_i = \mathbf{Q}_i \mathbf{U}_0 \mathbf{Q}_i^T$, $\mathbf{Q}_i \in \mathcal{P}_a$;
3. Solve the twinning equation to obtain the twinning system for all possible combinations of i, j : \mathbf{a} and \mathbf{h} : $\mathbf{R}\mathbf{U}_j - \mathbf{U}_i = \mathbf{a} \otimes \mathbf{h}$;
4. Solve the habit plane equation to obtain the transformation system \mathbf{b} and \mathbf{m} for all possible combinations of i, j : $\mathbf{Q}(\mathbf{U}_i + (1 - \mu)\mathbf{a} \otimes \mathbf{h}) = \mathbf{I} + \mathbf{b} \otimes \mathbf{m}$.

The transformation systems obtained can be found in Table 1.

References

- [1] Lai A, Du Z, Gan CL et al (2013) Shape memory and superelastic ceramics at small scales. *Science* 341(6153):1505–1508
- [2] Du Z, Zeng XM, Liu Q et al (2015) Size effects and shape memory properties in zro2 ceramic micro-and nano-pillars. *Scripta Mater* 101:40–43
- [3] Lai A (2016) Shape memory ceramics in small volumes. PhD thesis, Massachusetts Institute of Technology
- [4] Zeng XM, Lai A, Gan CL et al (2016) Crystal orientation dependence of the stress-induced martensitic transformation in zirconia-based shape memory ceramics. *Acta Mater* 116:124–135
- [5] Du Z, Zeng XM, Liu Q et al (2017) Superelasticity in micro-scale shape memory ceramic particles. *Acta Mater* 123:255–263
- [6] Zeng X, Du Z, Schuh CA et al (2017) Enhanced shape memory and superelasticity in small-volume ceramics: a perspective on the controlling factors. *MRS Commun* 7(4):747–754
- [7] Birkby I, Stevens R (1996) Applications of zirconia ceramics. In: *Key Engineering Materials*, Trans Tech Publ, pp 527–552
- [8] Reyes-Morel PE, Cherng JS, Chen IW (1988) Transformation plasticity of ceo2-stabilized tetragonal zirconia polycrystals: II, pseudoelasticity and shape memory effect. *J Am Ceram Soc* 71(8):648–657
- [9] Crystal IR, Lai A, Schuh CA (2020) Cyclic martensitic transformations and damage evolution in shape memory zirconia: Single crystals vs polycrystals. *J Am Ceram Soc* 103(8):4678–4690
- [10] Zhao Z, Radovitzky R, Cuitino A (2004) A study of surface roughening in f.c.c. metals using direct numerical simulation. *Acta Mater* 52(20):5791–5804. <https://doi.org/10.1016/j.actamat.2004.08.037>
- [11] Zhao Z, Kuchnicki S, Radovitzky R et al (2007) Influence of in-grain mesh resolution on the prediction of deformation textures in fcc polycrystals by crystal plasticity FEM. *Acta Mater* 55(7):2361–2373. <https://doi.org/10.1016/j.actamat.2006.11.035>
- [12] Jerusalem A, Dao M, Suresh S et al (2008) Three-dimensional model of strength and ductility of polycrystalline copper containing nanoscale twins. *Acta Mater* 56:4647–4657. <https://doi.org/10.1016/j.actamat.2008.05.033>
- [13] Zhao Z, Ramesh M, Raabe D et al (2008) Investigation of three-dimensional aspects of grain-scale plastic surface deformation of an aluminum oligocrystal. *Int J Plast* 24(2278):2297. <https://doi.org/10.1016/j.ijplas.2008.01.002>
- [14] Roy U, McDowell DL, Zhou M (2021) Effect of grain orientations on fracture behavior of polycrystalline metals. *J Mech Phys Solids*. <https://doi.org/10.1016/j.jmps.2021.104384>
- [15] Ye H, Yang F, Pan Z et al (2021) Significantly improvement of comprehensive energy storage performances with lead-free relaxor ferroelectric ceramics for high-temperature capacitors applications. *Acta Mater* 203(116):484
- [16] Miyazaki S, Kawai T, Otsuka K (1982) Study of fracture in cu-al-ni shape memory bicrystals. *Le J de Phys Colloques* 43(C4):C4-813. <https://doi.org/10.1051/jphyscol:19824133>
- [17] Miyazaki S, Kawai T, Otsuka K (1982) On the origin of intergranular fracture in β phase shape memory alloys. *Scr Metall* 16(4):431–436. [https://doi.org/10.1016/0036-9748\(82\)90167-3](https://doi.org/10.1016/0036-9748(82)90167-3)
- [18] Creuziger A, Crone W (2008) Grain boundary fracture in cualni shape memory alloys. *Mater Sci Eng A* 498(1):404–411. <https://doi.org/10.1016/j.msea.2008.08.039>

- [19] Pang EL, McCandler CA, Schuh CA (2019) Reduced cracking in polycrystalline zro2-ceo2 shape-memory ceramics by meeting the cofactor conditions. *Acta Mater* 177:230–239
- [20] Pang EL, Olson GB, Schuh CA (2020) Role of grain constraint on the martensitic transformation in ceria-doped zirconia. *J Am Ceram Soc*
- [21] Crystal IR, Schuh CA (2020) Grain size-effect on intergranular cracking in shape memory zirconia during cyclic martensitic transformations. Available at SSRN 3681175
- [22] Hannink RH, Kelly PM, Muddle BC (2000) Transformation toughening in zirconia-containing ceramics. *J Am Ceram Soc* 83(3):461–487
- [23] Chevalier J, Gremillard L, Virkar AV et al (2009) The tetragonal-monoclinic transformation in zirconia: lessons learned and future trends. *J Am Ceram Soc* 92(9):1901–1920
- [24] Ball J, James R (1987) Fine phase mixtures as minimizers of energy. *Arch Ration Mech Anal* 100(1):13–52. <https://doi.org/10.1007/BF00281246>
- [25] Simha N (1997) Twin and habit plane microstructures due to the tetragonal to monoclinic transformation of zirconia. *J Mech Phys Solids* 45(2):261–292. [https://doi.org/10.1016/S0022-5096\(96\)00074-9](https://doi.org/10.1016/S0022-5096(96)00074-9)
- [26] Kelly PM, Rose LF (2002) The martensitic transformation in ceramics: its role in transformation toughening. *Prog Mater Sci* 47(5):463–557. [https://doi.org/10.1016/S0079-6425\(00\)00005-0](https://doi.org/10.1016/S0079-6425(00)00005-0)
- [27] Bhattacharya K (2003) *Microstructure of martensite: why it forms and how it gives rise to the shape-memory effect*, vol 2, Oxford University Press, <https://doi.org/10.5860/choice.41-6554>
- [28] Gall K, Lim TJ, McDowell DL et al (2000) The role of intergranular constraint on the stress-induced martensitic transformation in textured polycrystalline niti. *Int J Plast* 16(10):1189–1214. [https://doi.org/10.1016/S0749-6419\(00\)0007-3](https://doi.org/10.1016/S0749-6419(00)0007-3)
- [29] Thamburaja P, Anand L (2001) Polycrystalline shape-memory materials: effect of crystallographic texture. *J Mech Phys Solids* 49(4):709–737. [https://doi.org/10.1016/S0022-5096\(00\)00061-2](https://doi.org/10.1016/S0022-5096(00)00061-2)
- [30] Thamburaja P, Anand L (2002) Superelastic behavior in tension-torsion of an initially-textured ti-ni shape-memory alloy. *Int J Plast* 18(11):1607–1617. [https://doi.org/10.1016/S0749-6419\(02\)00031-1](https://doi.org/10.1016/S0749-6419(02)00031-1)
- [31] Anand L, Gurtin M (2003) Thermal effects in the superelasticity crystalline shape-memory materials. *J Mech Phys Solids* 51:1015–1058. [https://doi.org/10.1016/S0022-5096\(03\)00017-6](https://doi.org/10.1016/S0022-5096(03)00017-6)
- [32] Dhala S, Mishra S, Tewari A et al (2019) Modeling of finite deformation of pseudoelastic niti shape memory alloy considering various inelasticity mechanisms. *Int J Plast* 115:216–237
- [33] Bowles J, Mackenzie J (1954) The crystallography of martensite transformations i. *Acta Metall* 2(1):129–137. [https://doi.org/10.1016/0001-6160\(54\)90102-9](https://doi.org/10.1016/0001-6160(54)90102-9)
- [34] Bowles J, Mackenzie JK (1954) The crystallography of martensite transformations iii. face-centred cubic to body-centred tetragonal transformations. *Acta Metall* 2(2):224–234. [https://doi.org/10.1016/0001-6160\(54\)90163-7](https://doi.org/10.1016/0001-6160(54)90163-7)
- [35] Mackenzie J, Bowles J (1954) The crystallography of martensite transformations ii. *Acta Metall* 2(1):138–147. [https://doi.org/10.1016/0001-6160\(54\)90103-0](https://doi.org/10.1016/0001-6160(54)90103-0)
- [36] Jin Y, Weng G (2000) Micromechanics study of thermo-mechanical characteristics of polycrystal shape-memory alloy films. *Thin Solid Films* 376(1–2):198–207
- [37] Niclaey C, Zineb TB, Arbab-Chirani S et al (2002) Determination of the interaction energy in the martensitic state. *Int J Plast* 18(11):1619–1647. [https://doi.org/10.1016/S0749-6419\(02\)00032-3](https://doi.org/10.1016/S0749-6419(02)00032-3)
- [38] Thamburaja P (2005) Constitutive equations for martensitic reorientation and detwinning in shape-memory alloys. *J Mech Phys Solids* 53(4):825–856. <https://doi.org/10.1016/j.jmps.2004.11.004>
- [39] Thamburaja P, Pan H, Chau F (2005) Martensitic reorientation and shape-memory effect in initially textured polycrystalline ti-ni sheet. *Acta Mater* 53(14):3821–3831. <https://doi.org/10.1016/j.actamat.2005.03.054>
- [40] Yu C, Kang G, Kan Q (2014) Crystal plasticity based constitutive model of niti shape memory alloy considering different mechanisms of inelastic deformation. *Int J Plast* 54:132–162
- [41] Siredey N, Patoor E, Berveiller M et al (1999) Constitutive equations for polycrystalline thermoelastic shape memory alloys. Part i. intragranular interactions and behavior of the grain. *Int J Solids Struct* 36:4289–4315. [https://doi.org/10.1016/S0020-7683\(98\)00196-6](https://doi.org/10.1016/S0020-7683(98)00196-6)
- [42] Patoor E, Eberhardt A, Berveiller M (1996) Micromechanical modelling of superelasticity in shape memory alloys. *Le J de Phys IV* 6(C1):C1-277. <https://doi.org/10.1051/jp4:1996127>
- [43] Gall K, Sehitoglu H (1999) The role of texture in tension-compression asymmetry in polycrystalline niti. *Int J Plast* 15(1):69–92. [https://doi.org/10.1016/S0749-6419\(98\)00060-6](https://doi.org/10.1016/S0749-6419(98)00060-6)
- [44] Gao H, Huang Y, Nix W et al (1999) Mechanism-based strain gradient plasticity i. theory. *J Mech Phys Solids* 47:1239–1263. [https://doi.org/10.1016/S0022-5096\(98\)00103-3](https://doi.org/10.1016/S0022-5096(98)00103-3)

- [45] Šittner P, Novák V (2000) Anisotropy of martensitic transformations in modeling of shape memory alloy polycrystals. *Int J Plast* 16(10):1243–1268. [https://doi.org/10.1016/S0749-6419\(00\)00009-7](https://doi.org/10.1016/S0749-6419(00)00009-7)
- [46] Gao X, Brinson LC (2002) A simplified multivariant sma model based on invariant plane nature of martensitic transformation. *J Intell Mater Syst Struct* 13(12):795–810. <http://doi.org/10.1177/1045389x02013012005>
- [47] Wang X, Xu B, Yue Z (2008) Micromechanical modelling of the effect of plastic deformation on the mechanical behaviour in pseudoelastic shape memory alloys. *Int J Plast* 24(8):1307–1332
- [48] Zaeem MA, Zhang N, Mamivand M (2019) A review of computational modeling techniques in study and design of shape memory ceramics. *Comput Mater Sci* 160:120–136
- [49] Zhang N, Zaeem MA (2016) Competing mechanisms between dislocation and phase transformation in plastic deformation of single crystalline yttria-stabilized tetragonal zirconia nanopillars. *Acta Mater* 120:337–347
- [50] Zhang N, Zaeem MA (2019) Understanding specimen-and grain-size effects on nanoscale plastic deformation mechanisms and mechanical properties of polycrystalline yttria-stabilized tetragonal zirconia nanopillars. *Eur J Mech A/Solids* 76:80–90
- [51] Zhang N, Zaeem MA (2020) Effects of grain orientations and pre-existing defects on mechanical properties and deformation mechanisms of polycrystalline yttria-stabilized tetragonal zirconia. *Materialia* 9(100):553
- [52] Zhang N, Zaeem MA (2020) Effects of twin boundaries and pre-existing defects on mechanical properties and deformation mechanisms of yttria-stabilized tetragonal zirconia. *J Eur Ceram Soc* 40(1):108–114
- [53] Artemev A, Jin Y, Khachaturyan A (2001) Three-dimensional phase field model of proper martensitic transformation. *Acta Mater* 49(7):1165–1177
- [54] Zhong Y, Zhu T (2014) Phase-field modeling of martensitic microstructure in niti shape memory alloys. *Acta Mater* 75:337–347
- [55] Cissé C, Zaeem MA (2020) An asymmetric elasto-plastic phase-field model for shape memory effect, pseudoelasticity and thermomechanical training in polycrystalline shape memory alloys. *Acta Mater* 201:580–595
- [56] Mamivand M, Zaeem MA, El Kadiri H (2014) Shape memory effect and pseudoelasticity behavior in tetragonal zirconia polycrystals: a phase field study. *Int J Plast* 60:71–86
- [57] Mamivand M, Zaeem MA, El Kadiri H (2015) Effect of variant strain accommodation on the three-dimensional microstructure formation during martensitic transformation: application to zirconia. *Acta Mater* 87:45–55
- [58] Moshkelgosha E, Mamivand M (2019) Anisotropic phase-field modeling of crack growth in shape memory ceramics: Application to zirconia. In: ASME International Mechanical Engineering Congress and Exposition, American Society of Mechanical Engineers, p V012T10A064
- [59] Noels L, Radovitzky R (2006) A general discontinuous Galerkin method for finite hyperelasticity. Formulation and numerical applications. *Int J Numer Methods Eng* 68(1):64–97. <https://doi.org/10.1002/nme.1699>
- [60] Noels L, Radovitzky R (2007) An explicit discontinuous Galerkin method for non-linear solid dynamics. Formulation, parallel implementation and scalability properties. *Int J Numer Methods Eng* 74(9):1393–1420. <https://doi.org/10.1002/nme.2213>
- [61] Radovitzky R, Seagraves A, Tupek M et al (2011) A scalable 3D fracture and fragmentation algorithm based on a hybrid, discontinuous Galerkin, Cohesive Element Method. *Comput Methods Appl Mech Eng* 200:326–344. <https://doi.org/10.1016/j.cma.2010.08.014>
- [62] Rengarajan G, Reddy J (2001) On the inelastic behavior of crystalline silicon at elevated temperatures. *J Mech Phys Solids* 49(8):1665–1700
- [63] Thamburaja P, Anand L (2003) Thermo-mechanically coupled superelastic response of initially-textured ti-ni sheet. *Acta Mater* 51(2):325–338. [https://doi.org/10.1016/S1359-6454\(02\)00389-0](https://doi.org/10.1016/S1359-6454(02)00389-0)
- [64] Kalidindi SR (1992) Polycrystal plasticity : constitutive modeling and deformation processing. PhD thesis, MIT, <http://hdl.handle.net/1721.1/13146>
- [65] Kuchnicki S, Cuitiño A, Radovitzky R (2006) Efficient and robust constitutive integrators for single-crystal plasticity modeling. *Int J Plast* 22:1988–2011. <https://doi.org/10.1016/j.ijplas.2006.02.008>
- [66] Kuchnicki S, Radovitzky R, Cuitiño A (2008) An explicit formulation for multiscale modeling of bcc metals. *Int J Plast* 24(12):2173–2191
- [67] Kisi EH, Howard CJ (1998) Elastic constants of tetragonal zirconia measured by a new powder diffraction technique. *J Am Ceram Soc* 81(6):1682–1684

Publisher's Note Springer Nature remains neutral with regard to jurisdictional claims in published maps and institutional affiliations.